RSC Advances

COMMUNICATION

Cite this: *RSC Adv.*, 2014, **4**, 32174

Received 13th May 2014
Accepted 2nd July 2014

DOI: 10.1039/c4ra04485a

www.rsc.org/advances

Solar H_2 generation *via* ethanol photoreforming on ε-Fe_2O_3 nanorod arrays activated by Ag and Au nanoparticles†

Giorgio Carraro,[a] Alberto Gasparotto,[a] Chiara Maccato,[a] Valentina Gombac,[b] Francesca Rossi,[c] Tiziano Montini,[b] Daniel Peeters,[ad] Elza Bontempi,[e] Cinzia Sada,[f] Davide Barreca*[g] and Paolo Fornasiero*[bh]

Earth-abundant, non toxic and cheap Fe_2O_3 can be used as photocatalyst for sustainable hydrogen production from bio-ethanol aqueous solutions, under sunlight irradiation and without the application of any external electrical bias. To this aim, supported materials are not only technologically more appealing than powders, but also of key importance to develop photoactive and stable Fe_2O_3-based nanostructured photocatalysts. Here we demonstrated that, while bulk Fe_2O_3 is unsuitable for solar hydrogen evolution, nanostructured iron(III) oxide polymorphs show promising photoactivity. In particular, a hydrogen yield of 20 mmol h^{-1} m^{-2} was obtained on ε-Fe_2O_3 nanorod arrays supported on Si(100) under simulated sunlight irradiation, mainly due to UV solar photon absorption. The functionalization with partially oxidized Ag nanoparticles resulted in a positive performance improvement upon selective irradiation with the UV portion of the solar spectrum. Conversely, the incorporation of Au nanoaggregates into ε-Fe_2O_3 enabled to obtain a significant H_2 production even under sole Vis light.

Hematite (α-Fe_2O_3) has been receiving constantly increasing attention as a non-inert support for water gas shift reaction (WGSR), preferential oxidation (PROX) or CO oxidation catalysts,[1,2] and, more recently, as a promising photoactive material in various energy-related applications, owing to its favorable chemical and physical properties, chemical stability in aqueous environments, non toxicity and high abundance.[3] As a relevant example, *hematite* has been widely investigated as photoanode in photoelectrochemical (PEC) cells for the sustainable conversion of sunlight into chemical energy through water splitting into O_2 and H_2.[4,5] Remarkably, a careful nanoscale design of *hematite* is the key step to obtain promising performances in water oxidation, circumventing its main disadvantages related to low light harvesting efficiencies and short photogenerated charge carrier lifetime.[3] Recently, the fabrication of supported iron(III) oxide nanomaterials proved the possibility of their applications not only in solar hydrogen production, but also in photoinduced hydrophilicity and photocatalytic pollutant oxidation, significantly broadening the potential perspectives for Fe_2O_3 technological applications.[6–8] In particular, ε-Fe_2O_3, a scarcely investigated iron(III) oxide polymorph,[9] grown in the form of supported pillars, shows good photocorrosion stability and promising activity in solar hydrogen production under 1.5 AM simulated solar irradiation in aqueous solutions containing alcohols.[6] In order to boost hydrogen yields and exploit the sustainable use of Vis light provided by the Sun, we investigated the effect of metal nanoparticles (NP) addition to ε-Fe_2O_3 nanorod arrays on solar hydrogen production. To this aim, we selected Ag and Au due to (i) their catalytic activity, (ii) the formation of metal-oxide Schottky junctions with Fe_2O_3, and (iii) the possibility of exploiting localized surface plasmon resonance (LSPR), ensuring a higher charge carrier lifetime and an improved Vis light absorption.[10–13]

Therefore, ε-Fe_2O_3 was deposited on Si(100) substrates *via* chemical vapor deposition (CVD), using $Fe(hfa)_2$TMEDA as a molecular source (hfa = 1,1,1,5,5,5-hexafluoro-2,4-pentanedionate; TMEDA = *N*,*N*,*N*′,*N*′-tetramethylethylenediamine).[14]

[a]*Department of Chemistry, Padova University and INSTM, Via Marzolo, 1-35131 Padova, Italy*

[b]*Department of Chemical and Pharmaceutical Sciences, ICCOM-CNR Trieste Research Unit – INSTM Research Unit, University of Trieste, via L. Giorgieri, 1-34127 Trieste, Italy. E-mail: pfornasiero@units.it*

[c]*CNR-IMEM, Parco Area delle Scienze, 43124 Parma, Italy*

[d]*Inorganic Chemistry II, Department of Chemistry and Biochemistry, Ruhr-University Bochum, 44801 Bochum, Germany*

[e]*Chemistry for Technologies Laboratory, Brescia University, 25123 Brescia, Italy*

[f]*Department of Physics and Astronomy, Padova University, Via Marzolo, 1-35131 Padova, Italy*

[g]*CNR-IENI and INSTM, Department of Chemistry, Padova University, Via Marzolo, 1-35131 Padova, Italy. E-mail: david.barreca@unipd.it*

[h]*King Abdullah University of Science and Technology, Thuwal 23955-6900, Saudi Arabia*

† Electronic supplementary information (ESI) available: Details of the synthesis procedures, material characterization and photocatalytic activity assessment; 2D-XRD patterns of the samples and related data; representative FE-SEM images of the ε-Fe_2O_3 material; XPS analysis of the samples; GC-MS analysis of the aqueous solutions after photocatalytic experiments. See DOI: 10.1039/c4ra04485a

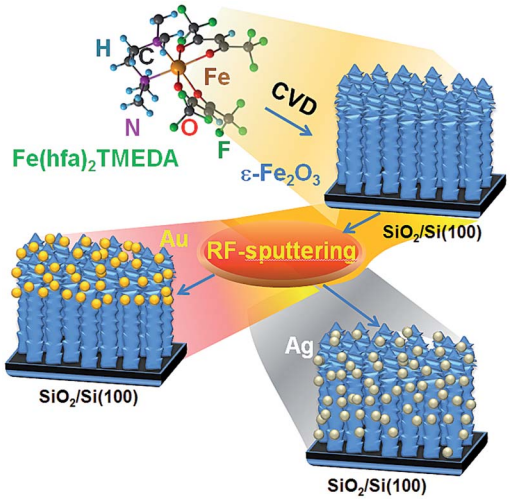

Scheme 1 Schematic representation of the adopted preparation protocol for the synthesis of ε-Fe_2O_3 nanosystems functionalized with Ag or Au nanoparticles.

Subsequently, silver and gold deposition on iron oxide samples was performed by a radio frequency (RF) plasmochemical reactor using electronic grade Ar (purity = 5.0) as plasma source. Finally, the obtained Ag/ε-Fe_2O_3 and Au/ε-Fe_2O_3 systems were annealed in air at 400 °C for 1 h [see Scheme 1 and ESI† for more details].

Two-dimensional X-ray diffraction [2D-XRD, Fig. S1 of the ESI†] images revealed the occurrence of single-phase ε-Fe_2O_3 [Pattern n°51122, Inorganic Chemical Structure Database (ICSD), 2007], free from other iron(III) oxide polymorphs (Table S1, ESI†). After Ag and Au introduction, no appreciable variations of the ε-Fe_2O_3 structure could be clearly observed, a phenomenon related to the mild conditions adopted for the sputtering processes, which, in turn, resulted in a high dispersion of Ag- and Au-containing aggregates.

Field emission-scanning electron microscopy (FE-SEM) micrographs (Fig. S2, ESI†) showed that iron oxide nanodeposits were characterized by homogeneous nanorod arrays grown perpendicular to the substrate surface. The nanorods, with an average diameter of 60 ± 20 nm, were assembled in a matrix with an overall thickness of 520 ± 30 nm. The obtainment of high aspect ratio (9 ± 3) nanorods with reduced lateral dimension results in a high active area and is advantageous to minimize charge carrier transport distances to the material surface, suppressing thus detrimental recombination losses. In addition, such systems represent ideal platforms for the subsequent functionalization with Ag and Au NPs, ensuring to the latter an intimate interfacial contact with Fe_2O_3 nanostructures, of great importance to improve functional performances.

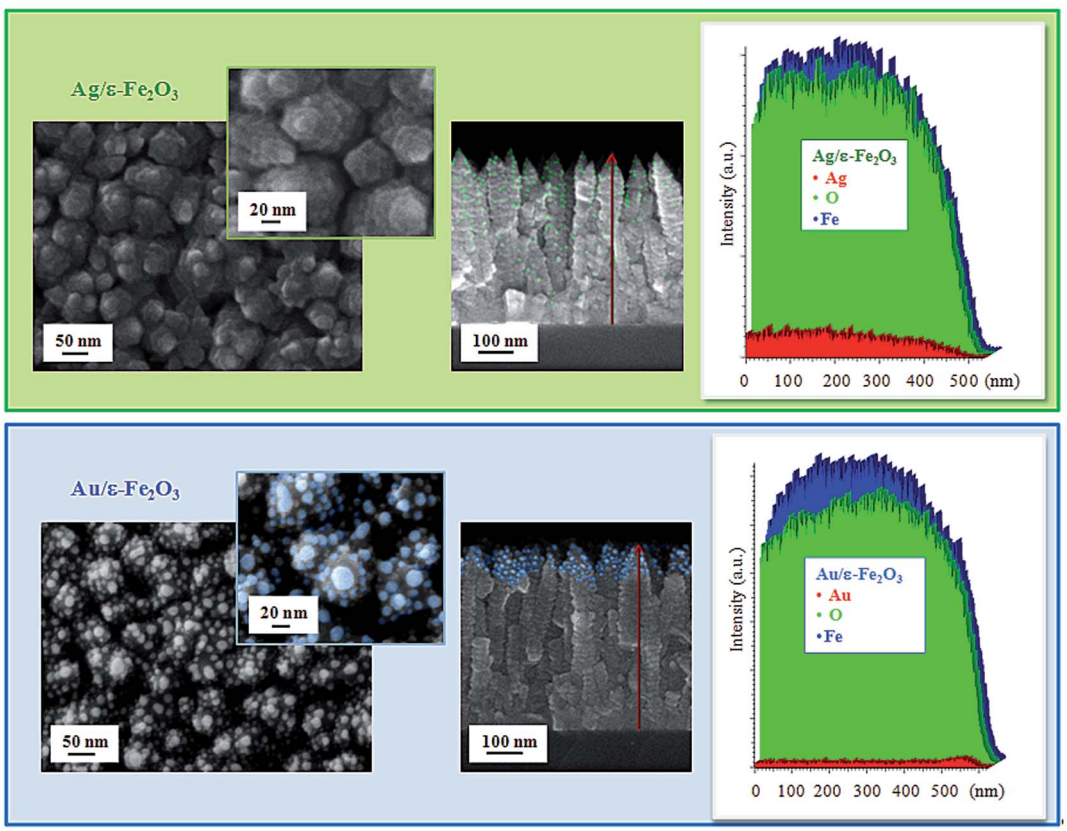

Fig. 1 Plane-view (left) and cross-sectional (center) FE-SEM micrographs for Ag/ε-Fe_2O_3 and Au/ε-Fe_2O_3 nanorod arrays, together with the corresponding EDXS line-scans (right) collected along the lines marked in the specimen cross-sectional views. Arrows indicate the direction of abscissa increase.

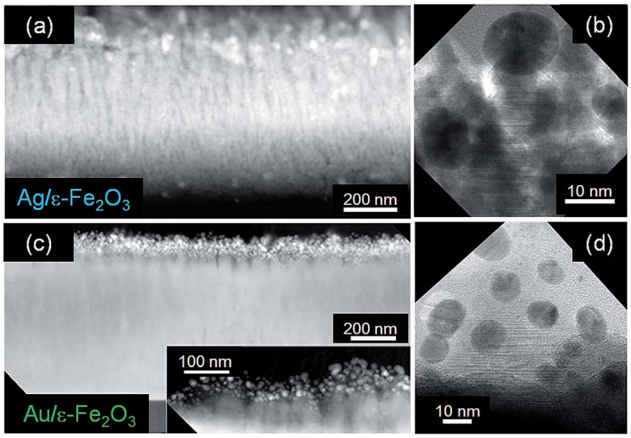

Fig. 2 Left panels: cross-sectional scanning TEM (STEM)-HAADF images of (a) Ag/ε-Fe_2O_3 and (c) Au/ε-Fe_2O_3 composite samples. The high-*Z* nanoparticles appear brighter than the matrix. Right panels: TEM images showing a detail of the sample surface with (b) Ag and (d) Au particles.

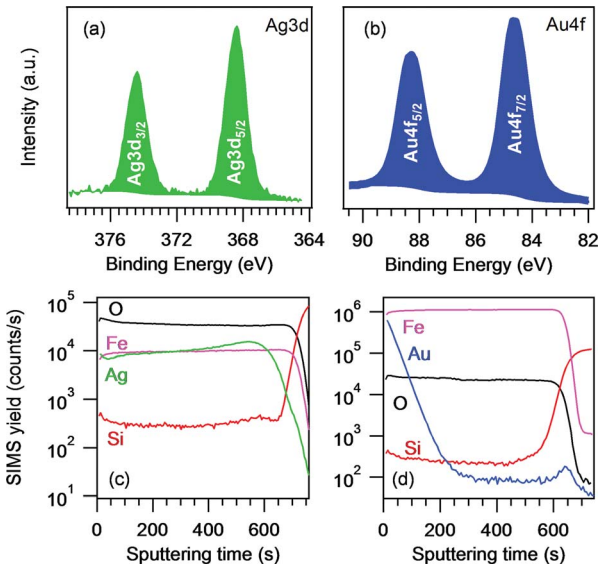

Fig. 3 (a) Ag3d and (b) Au4f photoelectron peaks for Ag/ε-Fe_2O_3 and Au/ε-Fe_2O_3 nanosystems. SIMS depth profiles for (c) Ag/ε-Fe_2O_3 and (d) Au/ε-Fe_2O_3 samples.

After RF-sputtering and thermal treatment, FE-SEM images (Fig. 1) showed that Ag and Au NPs were effectively dispersed on the surface of ε-Fe_2O_3 nanorod arrays, whose pristine morphology was preserved. Cross-sectional FE-SEM investigation coupled with energy dispersive X-ray spectroscopy (EDXS) line-scans evidenced a different in-depth dispersion for silver and gold particles, in spite of the very similar metal content (≈3 weight%) in the two samples. To attain a deeper insight into the spatial distribution of Ag and Au NPs inside the iron(III) oxide matrices, a transmission electron microscopy (TEM) investigation was carried out (Fig. 2). High angle annular dark field (HAADF) analyses showed that silver particles were distributed from the Fe_2O_3 surface down to the interface with the substrate (Fig. 2a). Conversely, gold particles were mainly confined in the material outermost regions, within a depth of ≈100 nm, corresponding to the nanorod tips (Fig. 2c and pertaining inset). Since EDXS measurements revealed an almost identical metal content for Ag and Au-containing samples, the different in-depth distributions observed for silver and gold nanoparticles can be traced back to the actual oxidation states of the two metals. In fact, XPS data (see below and Fig. 3a and b) pointed out to a partial Ag surface oxidation, resulting in the co-presence of Ag(0) and Ag(I) oxide. Conversely, gold was present only in its metallic state. The occurrence of surface Ag(I) oxide on silver NPs, resulting in a higher chemical affinity with ε-Fe_2O_3 matrices with respect to the case of Au, can be considered as the main responsible for the higher in-depth penetration of silver-containing nanoparticles.

Irrespective of the metal nature, high resolution TEM analyses (Fig. 2b and d) enabled to confirm that all the particles were crystalline and homogenously dispersed between ε-Fe_2O_3 nanorods. The average size of silver and gold NPs was 10 ± 4 and 15 ± 5 nm, respectively.

X-ray photoelectron spectroscopy (XPS, Fig. 3a, b and S3, ESI†) surface analyses evidenced the presence of iron, oxygen and, eventually, silver/gold, along with minor adventitious carbon contamination (<10.0 at%). The presence of iron(III) oxide free from other Fe oxidation states was confirmed by the Fe2p signal [binding energy (BE) ($Fe2p_{3/2}$) = 711.1 eV; spin–orbit splitting = 13.7 eV, Fig. S3b, ESI†],[9,15] whereas the O1s signal resulted from the concomitant contribution of lattice Fe_2O_3 oxygen (BE = 530.0 eV) and surface –OH species (BE = 531.8 eV, Fig. S3c of the ESI†).[16] Accordingly, the O/Fe atomic ratio was slightly higher than the expected stoichiometric value.

As concerns the deposited NPs, XPS analyses revealed a partial Ag surface oxidation [BE ($Ag3d_{5/2}$) = 368.4 eV, Fig. 3a], responsible for the co-presence of Ag(0) and Ag(I) oxide species.[15,16] In a different way, gold NPs showed the occurrence of the sole Au(0) [BE ($Au4f_{7/2}$) = 84.6 eV, Fig. 3b].[17] This BE value, ≈0.5 eV higher than the typical ones for metallic gold, resulted from both initial-state (charge exchange between gold and iron oxide) and final-state (relaxation and screening) phenomena, and evidenced the formation of Schottky junctions between Au NPs and ε-Fe_2O_3 nanorods.[11,18] The Ag and Au surface molar fractions (see ESI†) were X_{Ag} = 2% and X_{Au} = 54%, in line with the different distribution of Ag and Au NPs in the ε-Fe_2O_3 matrices evidenced by EDXS and TEM analyses (Fig. 1 and 2). To investigate the in-depth chemical composition, secondary ion mass spectrometry (SIMS) analyses were carried out. The data (Fig. 3c and d) revealed nearly parallel trends for Fe and O ionic yields, with well-defined interfaces with the substrate, confirming the homogeneity of the prepared ε-Fe_2O_3 matrices. Conversely, appreciable differences were observed in Ag and Au distribution. In fact, Ag NPs were evenly dispersed throughout the whole iron(III) oxide (Fig. 3c), whereas Au ionic yield displayed a progressively decreasing intensity with sputtering time, suggesting that gold was confined in the outermost material region, in line with the above observations.

Solar-driven hydrogen production from the target nanomaterials was achieved without any applied bias under

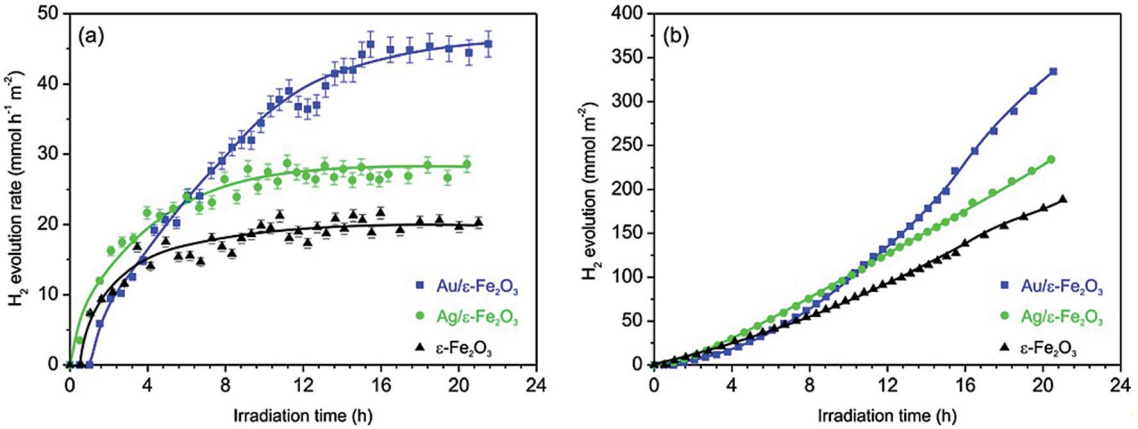

Fig. 4 (a) H_2 evolution rates and (b) integrated H_2 production from ethanol photoreforming on ε-Fe_2O_3, Ag/ε-Fe_2O_3 and Au/ε-Fe_2O_3 promoted by solar illumination.

simulated sunlight, from 1 : 1 water–ethanol solutions. No H_2 generation was observed in the absence of photocatalysts or without irradiation. Fig. 4 displays the H_2 evolution as a function of time, evidencing an appreciable reactivity coupled with a remarkable stability. The latter is further confirmed by the absence of detrimental photoleaching phenomena, previously observed in the case of α-Fe_2O_3-based photocatalysts.[6] Beside H_2 evolution, acetaldehyde and 1,2-diethoxyethane formation was detected in the liquid phase, whereas no CO_2 was observed in the gas phase. These evidences are consistent with the following mechanism, involving the initial ethanol adsorption on Fe_2O_3 surface:[19]

$$CH_3CH_2OH + 2^* \rightarrow CH_3CH_2O_{(ads)}{}^- + H_{(ads)}{}^+ \quad (1)$$

where * represents an adsorption site. Subsequently, the abstraction of a second hydrogen atom from ethoxide species *via* reaction with a photoproduced hole (h^+) results in acetaldehyde formation:

$$CH_3CH_2O_{(ads)}{}^- + h^+ + ^* \rightarrow CH_3CHO_{(ads)} + H_{(ads)}{}^+ + e^- \quad (2)$$

The weak acetaldehyde interaction with Fe_2O_3 surface leads to a fast desorption, preventing thus its further photooxidation. Consistently, no acetic acid or CO_2 could be detected. In the liquid phase, ethanol and acetaldehyde established an equilibrium, resulting in 1,2-diethoxyethane formation (see Fig. S4 of the ESI†). Finally, proton reduction leads to the formation of molecular hydrogen:

$$2H_{(ads)}{}^+ + 2e^- \rightarrow H_{2(ads)} \rightarrow H_{2(g)} \quad (3)$$

The technological importance of the actual performances is strengthened by the use of supported nanomaterials, enabling to circumvent filtration/sintering problems associated to powdered photocatalysts. In addition, the fabrication of supported nanostructures appears to be a key requirement to ensure solar-driven photoactivity. In fact, we prepared unsupported bulk α- and β-Fe_2O_3 polymorphs according to ref. 20 and 21, obtaining no H_2 production under the same experimental conditions, at variance with the corresponding supported nanosystems.[6] Therefore, the present results highlight the critical role of iron(III) oxide morphology and phase composition (ε-Fe_2O_3 in this case), which, on the other hand, cannot be obtained in bulk-unsupported forms.[22] We recently showed that the conduction band (CB) edge of nanostructured ε-Fe_2O_3 films is more positive than the potential of the H^+/H_2 redox couple at pH = 0.[6] Nevertheless, it is worth noting that the estimated CB edge position represents an average situation for the whole nanomaterial, which, in the present case, is composed of columnar structures and sharp tips. Specifically, the latter might show a shift of the CB edge to or above RHE due to their peculiar nanostructure, favourably contributing to proton reduction processes leading to H_2 evolution, as recently reported for CoO photocatalysts.[23] Consistently, elegant and recent *ab initio* calculations on Fe_2O_3 indicate the suitability of this materials for water splitting only in nanostructured forms.[24] In fact, whereas the conduction band edge of bulk Fe_2O_3 is below the H^+/H_2 redox potential, nanostructuring iron(III) oxides results in a progressive shift of its position above the H^+/H_2 redox potential, enabling thus adsorbed proton reduction.[24] In addition, it must be noted that the present experiments were carried out in nearly neutral solutions (pH ≈ 7) and at room temperature, more favourable conditions for proton reduction.[6]

Regarding composite materials containing metal-based NPs, Fig. 4 evidences that the introduction of both Ag and Au NPs results in enhanced H_2 yields with respect to bare ε-Fe_2O_3 deposit. A more detailed data inspection reveals that Ag/ε-Fe_2O_3 nanosystem shows an almost linear increase of H_2 concentration with illumination time (with a steady state H_2 production of 24.0 mmol h^{-1} m^{-2}, compared to 20.0 mmol h^{-1} m^{-2} for the bare ε-Fe_2O_3). In a different way, Au/ε-Fe_2O_3 system presents a two-regime behaviour, characterized by an initial activation period (≈8 h) with activities similar to the other systems, followed by an increase leading to a final steady state production almost doubled (45.0 mmol h^{-1} m^{-2}) than the original ε-Fe_2O_3 system. This behaviour suggests the occurrence of an activation process that involves the gold particles themselves and/or the

Au/ε-Fe_2O_3 junction. Due to the mild reaction conditions, the occurrence of significant structural modifications appears unlikely. Therefore, the initial activation process can be reasonably related to the establishment of an equilibrium between adsorbed species in solution, including ethoxy species or aldehydes derived from partial ethanol photooxidation, and/or to a partial gold oxidation during the photo-reforming process. These issues will be the subject of a forthcoming study.

The present trend as a function of the adopted NP nature is further confirmed by solar-to-fuel efficiency (SFE) values calculated under simulated solar light, yielding 0.07%, 0.09% and 0.17% for ε-Fe_2O_3, Ag/ε-Fe_2O_3 and Au/ε-Fe_2O_3, respectively. In spite of the fact that absolute values are not very high, the observed trend indicates a clear dependence of the system activity on the nature of the introduced NPs. In order to elucidate the role played by the latter, photocatalytic experiments were also carried out by using only the Vis portion of the solar spectrum (cut-off filter at 420 nm). Under these conditions, no H_2 evolution was observed for Ag/ε-Fe_2O_3 and ε-Fe_2O_3, despite ε-Fe_2O_3 can absorb an appreciable fraction of Vis light (E_G = 2.2 eV),[10] suggesting that the catalytic activity of these systems is essentially associated to the small fraction of UV photons in the solar spectrum (≈4%). We observed a similar behavior also in the case of supported α-Fe_2O_3,[6] a polymorph for which the presence of an indirect bang gap in the Vis and a direct band gap in the UV region is well documented.[3] The lower efficiency in photogeneneration of charge carriers in the case of an indirect bang gap can explain the poor performances under Vis irradiation, *i.e.* H_2 production below detection limits.

In a different way, Au/ε-Fe_2O_3 shows an appreciable hydrogen yield (8.0 mmol h^{-1} m^{-2}, SFE = 0.03%). These results demonstrate that the functionalization with metal NPs represents a strategic tool for the exploitation of a larger region of the solar spectrum.

The present data clearly highlight that both the nature and chemical state of the NPs affect the final performances. As a matter of fact, Au NPs of the present size are expected to be catalytically inactive, but the main role of Au nanoparticles in the present materials is not to act as catalyst themselves. Indeed, the formation of Schottky junctions with an intimate contact between the metal NPs and metal oxide matrix, such as in Au/ε-Fe_2O_3 nanosystem, is effective in promoting an efficient harvesting and management of Vis light, thanks to an improved separation of photogenerated charge carriers and to their efficient delivery to reactants involved in the photocatalytic process.[13,25,26] In the present case, two different processes can occur on Au/ε-Fe_2O_3. The first involves UV photon absorption by ε-Fe_2O_3, resulting in the formation of electron–hole pairs. Subsequently, photoelectrons can be efficiently transferred from ε-Fe_2O_3 to Au nanoparticles (thanks to the formation of a Schottky junction), limiting detrimental charge recombination. Proton reduction can occur on metal NPs, whereas holes remain on ε-Fe_2O_3, promoting ethanol photooxidation to acetaldehyde, as observed by gas chromatography (GC) analysis (Fig. S4 and Scheme S1a of the ESI†). In addition to this conventional metal–semiconductor photocatalysis, the presence of plasmonic gold nanoparticles, characterized by LSPR phenomena, enhance visible light absorption and further contribute to the observed activity by electron transfer from the metal to the semiconductor (Scheme S1b of the ESI†).[13,26] It is worthwhile noticing that the occurrence of such phenomena is strongly related to the nanometric dimensions of gold aggregates, that guarantee efficient LSPR in the visible range, and to the metallic state of NPs.

At variance with the Au case, Ag shows a lower efficiency in promoting H_2 production under simulated solar irradiation, and no appreciable activity under Vis light, a behaviour that is traced back to its different oxidation state. In fact, in the case of Ag/ε-Fe_2O_3 nanocomposite, the partial Ag surface oxidation to Ag_2O proved by XPS studies prevents the formation of a metal-iron(III) oxide Schottky junction and precludes contribution from LSPR, resulting in lower performances with respect to Au/ε-Fe_2O_3 case. Under solar simulator irradiation, the presence of UV and ethanol could contribute to partial Ag_2O reduction, as observed for other supported metals.[27] Nevertheless, this phenomenon should be limited to smaller nanoparticles, a minor fraction of those present in the investigated materials. The eventual presence of some metallic Ag NPs would lead to an absorption around 420–440 nm, due to their LSPR.[28,29] The proximity to the visible light cut-off would in any case technically limit this contribution. It is also worth noting that, whereas Au NPs mostly concentrate on the top of columnar ε-Fe_2O_3 arrays taking advantage of an optimal Vis light absorption, Ag-containing aggregates are evenly distributed throughout the entire Fe_2O_3 thickness, resulting thus in a less efficient light harvesting and, ultimately, in lower performances.

Conclusions

In summary, the present work has reported on a vapor-phase approach to M/Fe_2O_3 nanocomposites (M = Ag, Au) based on the scarcely investigated ε-Fe_2O_3 polymorph. Functionalization with Ag/Au yielded a high dispersion of metal-based NPs into the oxide matrix, with a spatial distribution and chemical state dependent on the nature of the metal itself. Notably, the ε-Fe_2O_3 high surface-to-volume ratio, along with the intimate metal/oxide contact, resulted in attractive performances in sunlight-assisted H_2 generation from ethanol–water solutions in the absence of any bias. Considering that one of the main actual bottlenecks is represented by an efficient harvesting of the whole solar spectrum for H_2 photoproduction, the present work has demonstrated the potential of introducing metal NPs in order to solve this issue. The proposed strategy, disclosing interesting perspectives for the fabrication of efficient metal oxide photocatalysts functionalized with suitable metal activators, holds a remarkable potential not only in photoassisted hydrogen evolution, but also in other photoactivated processes exploiting the direct use of solar light.

Acknowledgements

G.C, A.G., C.M., D.P., D.B. thank the European Community's Seventh Framework Program (FP7/2007–2013) under grant

agreement no. ENHANCE-238409. The authors also kindly acknowledge the financial support under the FP7 project "SOLAROGENIX" (NMP4-SL-2012-310333), as well as from Regione Lombardia-INSTM ATLANTE and Padova University ex-60% 2012–2013, SOLLEONE (CPDR132937/13) and PRAT 2010 (n° CPDA102579) projects. V.G., T.M. and P.F. acknowledge financial support from Trieste University through FRA 2013 project, as well as from Regione Lombardia-INSTM ATLANTE, HI-PHUTURE (protocol 2010N3T9M4) and COST Action 1104. Thanks are also due to Dr V. Longo and Prof. W.M.M. Kessels (Department of Applied Physics, Eindhoven University of Technology, The Netherlands) for useful assistance and scientific discussions.

Notes and references

1 Y. Zheng, Y. Cheng, Y. Wang, F. Bao, L. Zhou, X. Wei, Y. Zhang and Q. Zheng, *J. Phys. Chem. B*, 2006, **110**, 3093.
2 M. M. Schubert, A. Venugopal, M. J. Kahlich, V. Plzak and R. J. Behm, *J. Catal.*, 2004, **222**, 32.
3 K. Sivula, F. Le Formal and M. Grätzel, *ChemSusChem*, 2011, **4**, 432.
4 A. Kay, I. Cesar and M. Grätzel, *J. Am. Chem. Soc.*, 2006, **128**, 15714.
5 A. P. Singh, A. Mettenbörger, P. Golus and S. Mathur, *Int. J. Hydrogen Energy*, 2012, **37**, 13983.
6 G. Carraro, C. Maccato, A. Gasparotto, T. Montini, S. Turner, O. I. Lebedev, V. Gombac, G. Adami, G. Van Tendeloo, D. Barreca and P. Fornasiero, *Adv. Funct. Mater.*, 2014, **24**, 372.
7 G. Carraro, D. Barreca, D. Bekermann, T. Montini, A. Gasparotto, V. Gombac, C. Maccato and P. Fornasiero, *J. Nanosci. Nanotechnol.*, 2013, **13**, 4962.
8 D. Barreca, G. Carraro, A. Gasparotto, C. Maccato, F. Rossi, G. Salviati, M. Tallarida, C. Das, F. Fresno, D. Korte, U. Lavrenčič Štangar, M. Franko and D. Schmeisser, *ACS Appl. Mater. Interfaces*, 2013, **5**, 7130.
9 G. Carraro, C. Maccato, E. Bontempi, A. Gasparotto, O. I. Lebedev, S. Turner, L. E. Depero, G. Van Tendeloo and D. Barreca, *Eur. J. Inorg. Chem.*, 2013, 5454.
10 D. Barreca, G. Carraro, V. Gombac, A. Gasparotto, C. Maccato, P. Fornasiero and E. Tondello, *Adv. Funct. Mater.*, 2011, **21**, 2611.
11 Y. Pan, Y. Gao, G. Wang, D. Kong, L. Zhang, J. Hou, S. Hu, H. Pan and J. Zhu, *J. Phys. Chem. C*, 2011, **115**, 10744.
12 E. Thimsen, F. Le Formal, M. Grätzel and S. C. Warren, *Nano Lett.*, 2011, **11**, 35.
13 X. Zhang, Y. L. Chen, R. S. Liu and D. P. Tsai, *Rep. Prog. Phys.*, 2013, **76**, 046401.
14 D. Barreca, G. Carraro, A. Devi, E. Fois, A. Gasparotto, R. Seraglia, C. Maccato, C. Sada, G. Tabacchi, E. Tondello, A. Venzo and M. Winter, *Dalton Trans.*, 2012, **41**, 149.
15 G. Carraro, D. Barreca, E. Comini, A. Gasparotto, C. Maccato, C. Sada and G. Sberveglieri, *CrystEngComm*, 2012, **14**, 6469.
16 J. F. Moulder, W. F. Stickle, P. W. Sobol and K. D. Bomben, *Handbook of X-ray Photoelectron Spectroscopy*, Eden Prairie, Minnesota, 1992.
17 J. Zhang, X. Liu, L. Wang, T. Yang, X. Guo, S. Wu, S. Wang and S. Zhang, *J. Phys. Chem. C*, 2011, **115**, 5352.
18 A. Comin, K. Korobchevskaya, C. George, A. Diaspro and L. Manna, *Nano Lett.*, 2012, **12**, 921.
19 P. Pichat, M. Mozzanega and H. Courbon, *J. Chem. Soc., Faraday Trans. 1*, 1987, **83**, 697.
20 W. Hamd, S. Cobo, J. Fize, G. Baldinozzi, W. Schwartz, M. Reymermier, A. Pereira, M. Fontecave, V. Artero, C. Laberty-Robert and C. Sanchez, *Phys. Chem. Chem. Phys.*, 2012, **14**, 13224.
21 A. Kumar and A. Singhal, *Nanotechnology*, 2007, **18**, 475703.
22 M. Gich, A. Roig, E. Taboada, E. Molins, C. Bonafos and E. Snoeck, *Faraday Discuss.*, 2007, **136**, 345.
23 L. Liao, Q. Zhang, Z. Su, Z. Zhao, Y. Wang, Y. Li, X. Lu, D. Wei, G. Feng, Q. Yu, X. Cai, J. Zhao, Z. Ren, H. Fang, F. Robles-Hernandez, S. Baldelli and J. Bao, *Nat. Nanotechnol.*, 2014, **9**, 69.
24 M. C. Toroker, D. K. Kanan, N. Alidoust, L. Y. Isseroff, P. Liao and E. A. Carter, *Phys. Chem. Chem. Phys.*, 2011, **13**, 16644.
25 A. Primo, A. Corma and H. García, *Phys. Chem. Chem. Phys.*, 2011, **13**, 886.
26 C. G. Silva, R. Juárez, T. Marino, R. Molinari and H. García, *J. Am. Chem. Soc.*, 2011, **133**, 595.
27 T. Montini, V. Gombac, L. Sordelli, J. J. Delgado, X. Chen, G. Adami and P. Fornasiero, *ChemCatChem*, 2011, **3**, 574.
28 S. Peng, J. M. McMahon, G. C. Schatz, S. K. Gray and Y. G. Sun, *Proc. Natl. Acad. Sci. U. S. A.*, 2010, **107**, 14530.
29 M. A. H. Muhammed, F. Aldeek, G. Palui, L. Trapiella-Alfonso and H. Mattoussi, *ACS Nano*, 2012, **6**, 8950.